

Failure analysis of AISI 430 stainless-steel sheet under stretching and bending conditions

VALMIR DIAS LUIZ (✉ valmir_dl@yahoo.com.br)

UFMG: Universidade Federal de Minas Gerais <https://orcid.org/0000-0001-8078-587X>

Paulo César de Matos Rodrigues

Research Article

Keywords: test conditions, Nb-stabilized AISI 430 stainless steel sheet, bending under tension test, strip-tension test, coefficient of friction

Posted Date: March 11th, 2022

DOI: <https://doi.org/10.21203/rs.3.rs-1427473/v1>

License:  This work is licensed under a Creative Commons Attribution 4.0 International License.

[Read Full License](#)

Failure analysis of AISI 430 stainless-steel sheet under stretching and bending conditions

Valmir Dias Luiz^{1,2,*}, Paulo César de Matos Rodrigues^{1†}

¹ Graduate Program in Mechanical Engineering, Universidade Federal de Minas Gerais, Av. Antônio Carlos, 6627, Pampulha, Belo Horizonte 31270-901, MG, Brazil

² Department of Metallurgy and Chemistry, Centro Federal de Educação Tecnológica de Minas Gerais, R. 19 de Novembro, 121, Centro Norte, Timóteo 35180-008, MG, Brazil

*Corresponding author(s). E-mail(s): valmir_dl@yahoo.com.br; valmir@cefetmg.br;

†Contributing author: paulocmr@ufmg.br

†This author contributed equally to this work.

ORCID of the author(s):

Luiz VD - <https://orcid.org/0000-0001-8078-587X>

Rodrigues PCM - <https://orcid.org/0000-0001-6386-6029>

Abstract

Ferritic stainless steels have been widely used to substitute austenitic steels because of their lower cost and higher deep drawing capacity. However, failures, such as shear fracture, have been observed in parts with small radii during the drawing process in applications where both bending and stretching occurs. Conventional techniques, such as failure criterion consideration, finite element method, and forming limit diagram, are unable to predict this type of fracture, which has hampered the development of new processes and products. To overcome this limitation, herein, we investigated the effects of tool radius, direction, and test speed on the formability to fracture of an AISI 430 stainless-steel sheet under bending and stretching conditions. An equipment was used to perform the draw-bend fracture (DBF) test based on the bending under tension test. The DBF test efficiently reproduced the tensile, mixed, and shear fractures. Furthermore, we determined the fracture limit strain on the outer surface, thickness, and sidewall of the sample, as well as the coefficient of friction. The data showed that the radius to thickness ratio related to the process parameters had a direct impact on the experimental results. In addition, the results can be utilized for setting design guidelines and failure prevention.

Key words: test conditions, Nb-stabilized AISI 430 stainless steel sheet, bending under tension test, strip-tension test, coefficient of friction

1 Introduction

Ferritic stainless steels (FSSs) are metallic alloys based on Fe-Cr with the $\langle \text{Cr} \rangle$ content of 10.5–27%, which exhibit high corrosion resistance and possess long shelf life [1,2]. In recent years, FSSs have been widely used in various industries (e.g., civil, home appliances, food, pharmaceutical, chemical, bioengineering, and automotive) as an alternative to austenitic stainless steels, mainly because of their lower cost and excellent ability for deep drawing. In addition, they have lower thermal expansion, higher thermal conductivity, higher resistance to oxidation at high temperatures, and are not hardened by heat treatment, but by cold working [3,4].

However, one of the considerable challenges of these and other metal alloys is the successful stamping of parts, which requires having excellent surface appearance, minimal material consumption, high productivity, low tool wear, and absence of fractures. Over the years, researchers around the world have devoted efforts to primarily mitigate failures during the sheet metal forming (SMF) process, as this has been the main barrier for the wide-scale use of new materials and materials with specific properties [5-11]. It can be seen in Fig. 1a that the AISI 430 FSS failed in applications where the ratio of the tool radius to plate thickness (R/t) was small. Filho et al. [12] also observed this type of failure during a deep drawing operation.

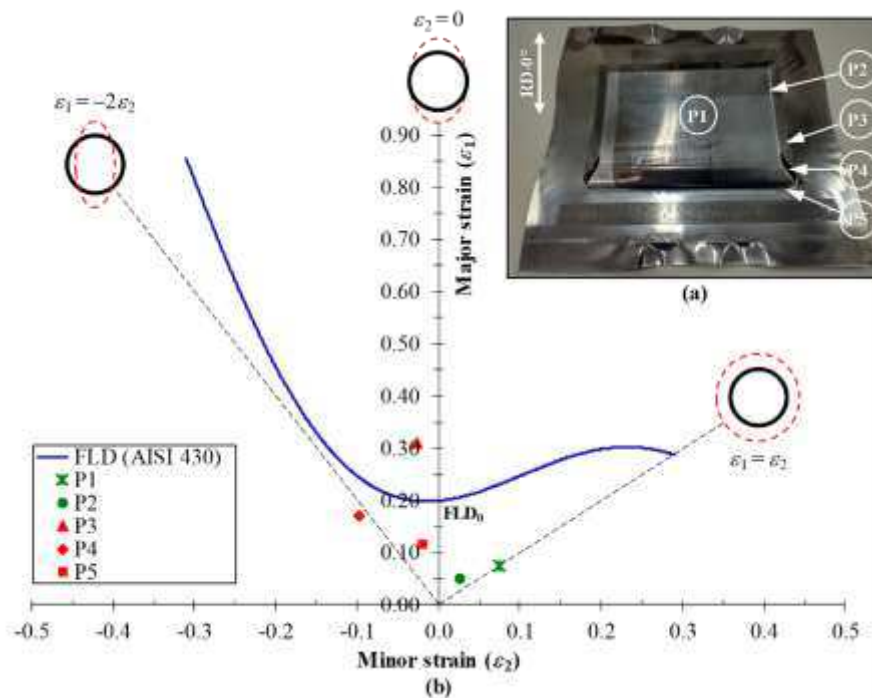


Fig. 1 (a) Fractures in an example-part with AISI 430 steel; (b) Forming Limit Diagram (FLD). RD-0° is the sheet rolling direction

This type of failure contrasts the crystalline texture of the material. Many studies have emphasized the excellent deep drawing capacity of the AISI 430 steel owing to the cold rolling texture in the center of the sheet [13,14]. Damborg [15] revealed that most conventional low-C alloys typically fail in response to stretching in regions under plane-strain or with soft radii. This type of failure is characterized as a shear fracture because it occurs in parts with small radii under low load with little or no apparent necking, in contrast to a tensile fracture. To date, this behavior has only been investigated in advanced high strength steels (AHSSs), but not in FSSs. Among the materials investigated is the DP590 steel, which has a formability similar to that of the AISI 430 steel. Several authors have performed a series of studies on the shear fracture in AHSSs and concluded that a critical R/t for each test material exists between the safe and fail zones occurring during stretch bending [7,9,16-18].

Ghosh and Hecker [19] observed that the bending on deformation has a positive influence SMF processes. However, Baudelet e Ragab [20] experimental investigated the Out-of-plane and in-plane stretch, and concluded that it is found that the former method produces higher limit strains than the latter under identical degrees of strain biaxiality and initial sheet thickness. Cheong [21] explained that the superposition of stretching and bending can lead to a nonlinear deformation path. Currently available techniques, such as failure criterion consideration, finite element analysis (FEA), and FLD, are based on localized strain before fracture; therefore, they are unable to predict the shear fracture in parts with small radii because there is almost no necking. Supporting these arguments, it can be seen in Fig. 1a and b, that the fracture limit strain on the outer surface of the example-part in the plane region (point P3) was above FLD0; on the other hand, in the regions with small radii (points P4 and P5), fracture limit strain was below FLD0, i.e., the fracture occurred in a region initially considered safe to stamp the part, denoting that the FLD method was ineffective in predicting faults in regions with small radii of parts.

Accordingly, experimental methods have been the most effective in the reproduction, characterization, and analysis of this type of failure. However, there are few mechanical tests capable of reliably reproducing the shear fracture of metal sheets with small radii of the punch and die in a laboratory environment. Over the years, several experimental tests have been developed to evaluate the formability of metal sheets under bending and stretching conditions, such as the angular stretch-bend test (ASBT) [22], modified Duncan-Shabel apparatus [16], bending under tension (BUT) test [23,24], and use of the stretch forming simulator (SFS) [17]. Among these, the latter two tests have been widely used because they accurately simulate the plastic strain mechanics of the sheet over the tool. Shih et al. [18] used the SFS and conducted the modified-BUT tests to reproduce shear fractures and observed that both fracture limit curves converged satisfactorily.

Originally, the BUT test was developed to simulate the contact and the deformation of a sheet metal at the die radius. During the test, a metallic strip is forced to slide over a fixed or free cylindrical pin using two independently controlled hydraulic actuators arranged at a 90° angle [23,24]. The strip is subjected to combined effect of the bending,

unbending, and stretching efforts [25]. Subsequently, Sung et al. [7] modified the BUT test to operate it at a wide range of stamping speeds and $R\dot{t}$ ratios, ensuring high consistency and reproducibility of results. This test became known as the tensile draw-bend fracture (DBF) test.

To date, no study has been conducted an analysis of the failures in AISI 430 steel under bending and stretching conditions, causing a gap in our knowledge related to the formability of this material. Therefore, the present work aimed to reproduce, characterize, and analyze the failures presented by this material under these deformation conditions. For this, an equipment based on the BUT test was used to perform the DBF test. In addition, process parameters, such as pin radius, direction, and test speed, were varied to investigate their effects on the fracture limit deformation on the outer surface, thickness, and sidewall of the sheet, as well as on the coefficient of friction value. The results were plotted as a function of the $R\dot{t}$ ratio and then compared, analyzed, and discussed.

2 Materials and Methods

2.1 Materials and samples preparation

The material investigated was an FSS AISI 430 plate with an initial thickness, t_0 , of 0.8 mm, and the bending pins were made of the AISI O1 steel. The steel sheet under the as-received condition was cold rolled, annealed, and pickled, with a slight skin pass. Its chemical composition is shown in Table 1.

Table 1 Chemical composition of the Nb-stabilized AISI 430 ferritic stainless steel (wt %)

C	Mn	Si	P	S	Ni	Cr	Mo	Nb	Ti	N (ppm)
0.0164	0.2454	0.2447	0.0362	0.0009	0.2964	16.481	0.0234	0.3384	0.0035	231

The surface roughness (Ra) of the samples and bending pins were measured with a portable rugosimeter, model Rugosurf 20 (Tesa SA, Renens, Switzerland), and the average results were 0.051 ± 0.010 μm and 0.270 ± 0.048 μm , respectively. Their hardness was determined using a Vickers microhardness tester, model HMV-2T (Shimadzu, Kyoto, and Japan), with a load of 4.9 N, and the average results were 158 ± 6 HV and 746 ± 11 HV, respectively.

The tensile mechanical properties of the AISI 430 steel were determined using a universal testing machine, model DL30000 (Instron/Emic, Massachusetts, USA). Three tensile samples, with geometry according to ASTM E8/E8M [26], were cut in three different directions (0° , 45° , and 90°) in relation to the original direction of sheet rolling using the wire electrical discharge machining, model EURO-EW1 (Eurostec, Caxias do Sul, Brazil). The mechanical properties of the

AISI 430 steel sheet are listed in Table 2. The procedures described by Banabic et al. [27] were used to determine coefficients n , r , r_b , and Δr .

Table 2 Tensile properties of the AISI 430 steel

Sample direction	S_y (MPa)	S_u (MPa)	e_u (%)	e_t (%)	n	r	r_b	Δr
0°	316.1	464.9	22.3	32.7	0.205	1.419		
45°	343.4	475.6	17.9	27.2	0.188	1.196	1.366	0.340
90°	317.5	466.5	19.8	33.2	0.201	1.654		

S_y = yield strength, S_u = ultimate tensile strength, e_u = uniform elongation, e_t = total elongation, n = coefficient of hardening, r = normal anisotropy coefficient, r_b = mean normal anisotropy coefficient, and Δr = planar anisotropy coefficient.

The samples used in the conformability tests were cut on a mechanical guillotine according to the geometry shown in Fig. 2a. However, notches that induced a plane deformation state were achieved using a waterjet cutting machine, model IFB-4137 (Flow Corp., Washington, USA). Subsequently, a deterministic grid of secant or interlaced circles (Fig. 2b) with 2.0 mm initial diameter, d_0 , was electrochemically deposited in the notched region of the samples for use of the circle grid analysis (CGA) method introduced by Keeler [28].

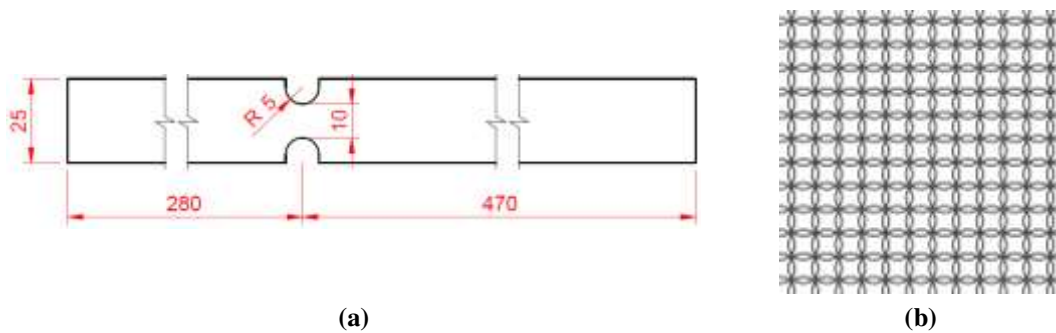


Fig. 2 Schematic representation of the (a) notched sample geometry (mm); (b) deterministic grid of secant circles

2.2 Draw-bend fracture (DBF) test

As shown in Fig. 3a, an apparatus based on the BUT test has been used in execution of DBF test. Its limit characteristics consist in the application of a force of 44.5 kN, a speed of 75 mm/s, and displacement of the hydraulic actuators by up to 250 mm. In addition, may performed conformability tests using free and fixed pins. As can be seen in Fig. 3b, a fixed pin

tool holder was specially designed to vary the radius of the bending pin in this study. The top surface of the pins was positioned at the intersection of the lines of action of the two hydraulic cylinders to maintain tangency at an angle of 90° .

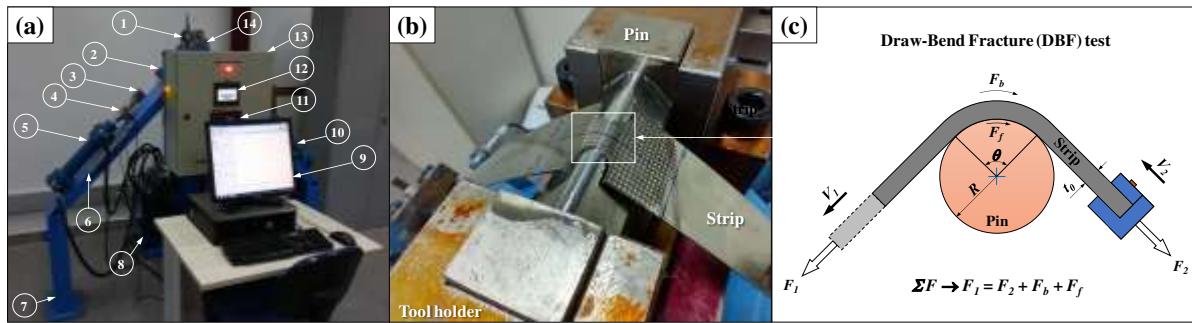


Fig. 3 (a) BUT test apparatus: 1. torque meter, 2. inductive proximity sensor, 3. grip, 4. load cell, 5. Front hydraulic cylinder, 6. LVDT position sensor, 7. assembly structure, 8. hydraulic power unit, 9. computer with application software, 10. back hydraulic cylinder, 11. torque meter, 12. human-machine interface, 13. control panel, and 14. free pin tool holder; (b) fixed tool holder; (c) schematic representation of the DBF test

As illustrated in Fig. 4, the data acquisition system (DAS) of the equipment used USB interface devices (Loadstar Sensors, Fremont, USA), which were responsible for the acquisition and signal processing of load and displacement sensors. This equipment still contained a meter and torque sensor, but it was used only in applications with free pins. With the aid of an application software (SensorVUE), these data were stored simultaneously on a computer. Subsequently, the graphs were plotted for an analysis of the results. Puroshit et al. [28] used a DAS similar to that shown in Fig. 4.



Fig. 4 Schematic representation of the DAS. Adapted from Loadstar Sensors [29]

Table 3 lists the operational parameters adopted in the DBF test. In each new test, the tribo-surfaces were cleaned with acetone, and then a mineral oil-based lubricant was applied abundantly using a silicone oil brush. Three samples were tested under each test condition to ensure the repeatability of the results.

Table 3 Operating parameters used in the DBF test

Operating parameters	Description
Sample direction*	RD-0° and TD-90°*
Test speed, v	2.5 and 25 mm/s
Bending pin radius, R	1.5, 3.0, 4.5, 6.0, 7.5, 9.0, 10.5, 13.5, 16.5, and 19.5 mm
Lubricant	viscosity (η) of 120 mPa.s and density (ρ) of 0.894 g/cm ³

*TD-90° is the transversal direction of sheet rolling.

2.3 Constitutive equations and fractured samples analysis

Figure 3c shows that the DBF test is based on the operating principle of the BUT test, wherein four components of forces are assumed during the sliding of the sheet under the bending pin's radius of curvature. Several authors [24,30,31] have explained that the force required to pull the strip (F_1) around the radius must overcome the three basic forces shown in the balance of the total forces shown in Eq. 1.

$$F_1 = F_2 + F_b + F_f \quad (1)$$

where F_1 is the frontal or pulling force, F_2 is the back or restraining force, F_b is the bending force, and F_f is the frictional force.

The fracture limit strain on the outer surface of the sheet (ε_{1f}), which occurred in the direction perpendicular to the fracture of the samples during the DBF test, was obtained by Eq. 2, as described by Silva et al. [32]. For CGA, we used the Zürich procedure n.5 presented by Parniere and Sanz [33], which evolved into the position-dependent method described by norm ISO 12004-2 [34]. To improve the accuracy of measuring the strains imposed on the samples, a digital microscope (up to 1000× magnification and 2.0 MP resolution) and Image-Pro Plus software (version 6.0) were used to capture images and measure the deterministic grid of secant circles (before and after the experimental tests), respectively.

$$\varepsilon_{1f} = \ln\left(\frac{l_{major}}{d_0}\right) \quad (2)$$

where l_{major} is the length of the major axis of the ellipses resulting from the longitudinal deformation of the secant circles.

The thickness reduction (R_f) and fracture limit strain in the sheet thickness (ε_{3f}) were determined using Eqs. 3 and 4, respectively, as reported by Nielsen and Martins [35]. The fracture thickness (t_f) was obtained using a digital micrometer with 0.001 mm precision, and its value corresponded to the average of five measurements at different locations in the fractured section of the sample. Since the deformation was compressive, its result was plotted in modulus for comparison purposes.

$$R_f = \frac{t_0 - t_f}{t_f} \quad (3)$$

$$\varepsilon_{3f} = \ln(1 - R_f) \quad (4)$$

The fracture limit strain on the sample wall due to stretching was determined by the ratio between the maximum length and initial of the notch, L_{max}/L_0 . L_{max} was obtained by an LVDT sensor attached to the front hydraulic cylinder rod of the apparatus shown in Fig. 3a. The morphology of the fracture surfaces was analyzed using a scanning electron microscope, model JSM-6510LV (Jeol, Tokyo, Japan) with an acceleration of 20 kV.

The COF (μ) was calculated using Eq. 5. This equation has been used for decades [30,36] in the tribology of SMF with cylindrical tools because it considers the geometric parameters of the tribological pair in the constitutive equation, such as the sheet thickness and tool radius.

$$\mu = \frac{2}{\pi} \left(1 + \frac{t_0}{2R}\right) \ln\left(\frac{F_1 - F_b}{F_2}\right) \quad (5)$$

The bending force (F_b) was determined using Eq. 6, as introduced by Swift [37]. The sample width (w) was assumed to be the notch width because the localized deformation was concentrated in this region.

$$F_b = \frac{S_y t_0^2 w}{2R} \quad (6)$$

3 Results and Discussion

3.1 Characterization of fracture types

Figure 5a show the schematic representation of deep drawing process and Figs. 5b–d shows the different types of fractures that were reproduced during the DBF test: tensile, mixed, and shear fractures. These fractures were designated as types 1, 2, and 3, respectively. A condition of plane-strain was assumed during the experimental tests of the samples. The experimental results showed that as radius/thickness (R/t) ratio revealed, fracture tends to move from the curvature region to the flat region of the sheet.

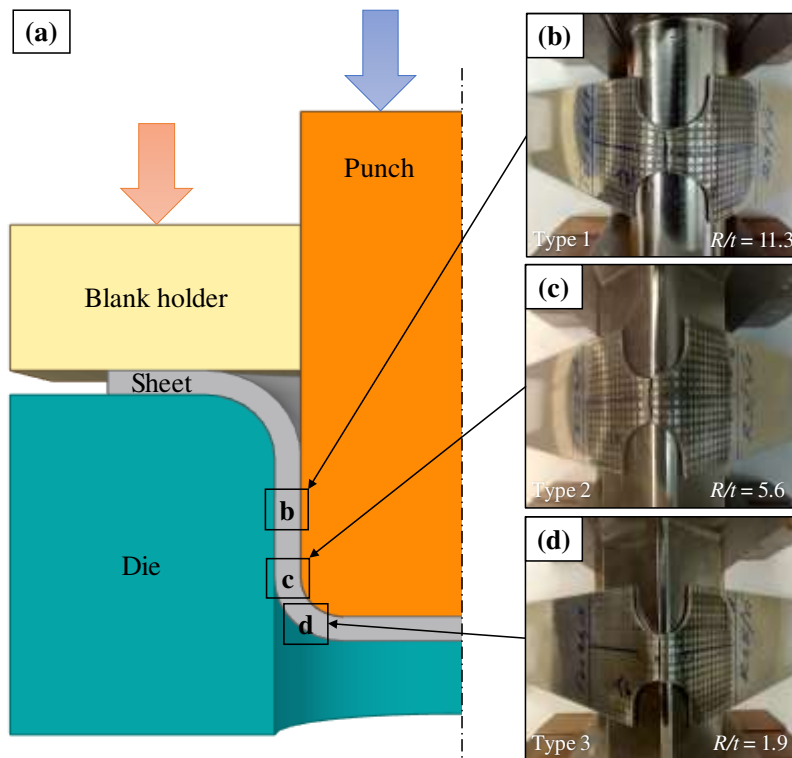


Fig. 5 Different fracture types reproduced in the DBF test. (a) schematic representation of deep drawing process; (b) type 1 (tensile fracture at sidewall); (c) type 2 (mixed fracture at the tangent point); (d) type 3 (shear fracture in the punch radius)

Figures 5a and 5b show that type 1 is similar to the fracture that occurs in the sidewall of stamped parts. Generally, this failure is referred as ductile fracture and is observed in metallic materials in a conventional tensile test, as the fracture occurred when the sample-resistant section was reduced by localized deformation or necking. Dieter [38] explained that before the ductile fracture, the necking introduces a triaxial stress state, and a hydrostatic component of stress act at the center of the notch region until the sample reached its minimum dimensions (Fig. 6a) and, consequently, its final rupture.

A commonly accepted interpretation is that a tensile fracture originates from the initiation, growth, and coalescence of microscopic voids during plastic deformation [39]. This void nucleation generally occurs at the interfaces of inclusions and second-phase particles, and the dissociation of these interfaces is the dominant mechanism in void nucleation. These behaviors were confirmed by an interrupted tensile test, as shown in Fig. 7a. The fracture propagated from the center to the edges of the notch (Fig. 7b), and the morphological aspect of the fracture surface (Fig. 7c) was similar to that of the sample subjected to the DBF test (Fig. 6b). Both fracture surfaces were characterized by the presence of equiaxed dimples, which, from a macroscopic perspective, are normal to the direction of the applied force (F_1).

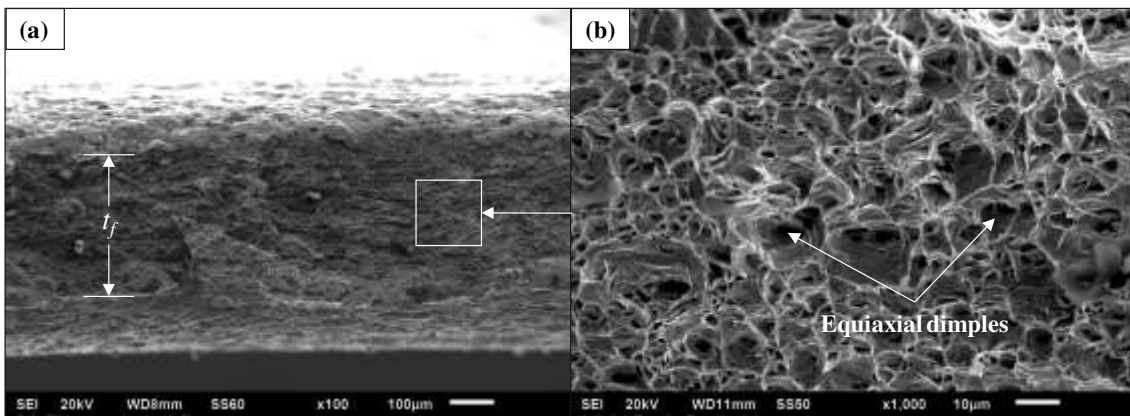


Fig. 6 SEM image of the tensile fracture (type 1). (a) macrographic aspect of the sample fracture; (b) morphological aspect of the fracture surface

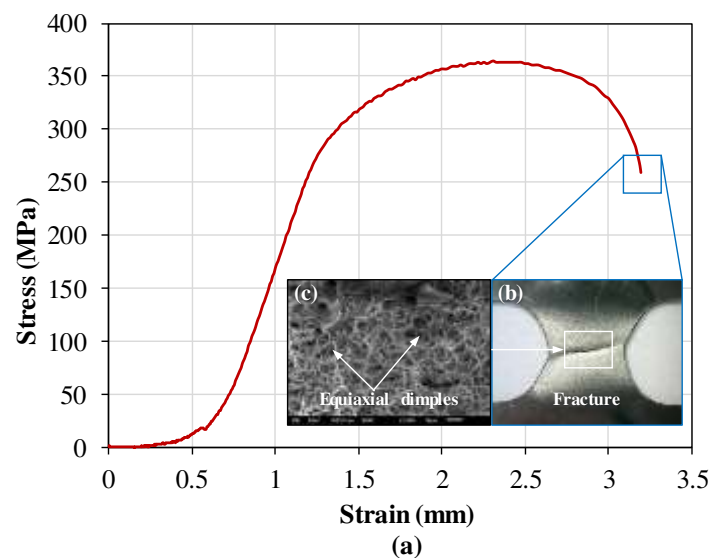


Fig. 7 Interrupted tensile test of a notched sample. (a) stress-strain curve of the AISI 430 steel; (b) macrographic image of fracture start; (c) SEM image of the fracture surface

In contrast, Figs. 5a and 5d show that type 3 tends to occur under the tool radius and is similar to brittle fracture, which, by definition, occurs with low energy absorption (i.e., with little or no macroscopic plastic deformation) under stresses lower than those corresponding to the generalized yielding, and with a significantly high crack-propagation velocity [38,39]. Furthermore, the fracture started at the edge of the sample and propagated perpendicularly to its longitudinal axis while its minimum dimensions (Fig. 8a) were still much larger than those of type 1 (Fig. 6a). Supporting these results, Martínez-Donaire et al. [40] demonstrated that the fracture initiation site was shifted closer to the sheet free-edge as the punch radius decreased and with low plastic strain. Figure 8b clearly shows that the fracture surface morphology contains sheared dimples or highly elongated, characteristics typical of those obtained in a shear fracture. The shear fracture mechanism during an SMF operation is not by pure shear as seen in sheet metal cutting, which would result in a flat surface practically without any significant topographic relief, but by sliding between crystallographic planes. The presence of cleavage facets on the fracture surface (Fig. 8b) supported these arguments, since they occurred due to the separation of the crystallographic planes by rupturing atomic bonds [41].

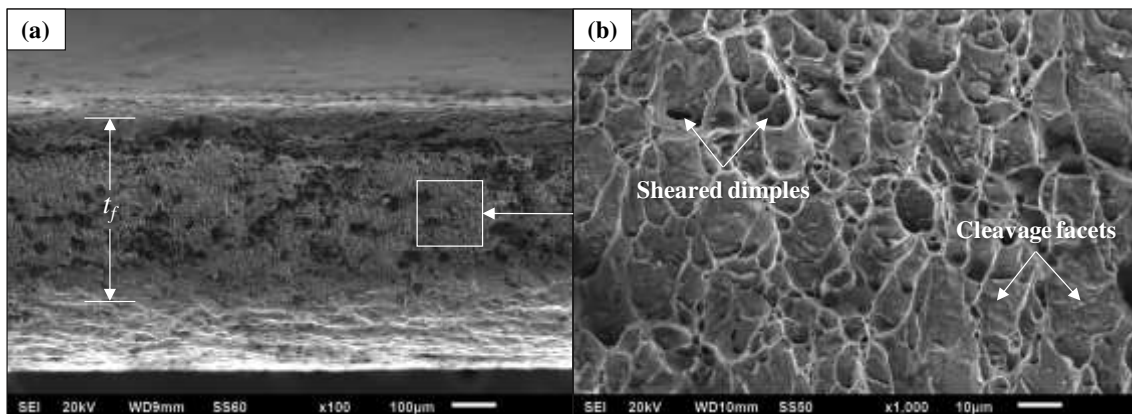


Fig. 8 SEM image of the shear fracture (type 3). (a) macrographic aspect of the sample fracture; (b) morphological aspect of the fracture surface.

A comparative analysis between Figs. 9b and 8b evidence that the failure occurred in the example-part is shear fracture, as both surfaces presented the same fracture mechanisms, i.e., sheared dimples and cleavage facets. This also indicated that the DBF test efficiently reproduced, in a laboratory environment, a fracture commonly observed in industrial practices, especially in the region of small radii of the punch.

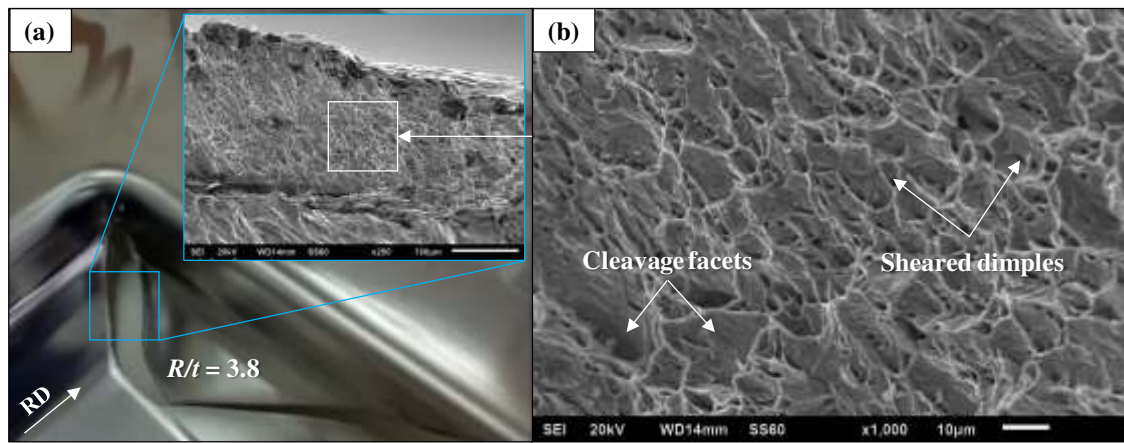


Fig. 9 (a) Macrographical aspect of the fracture in the example-part; (b) morphological aspect of the fracture surface

On the other hand, type 2 is called mixed because it occurs during the transition between a shear and tensile fracture. Figures. 5a and 5c show that this type of fracture tends to occur on the tangent point line between the side wall and punch radius. Sung et al. [7] explained that, in industrial practices, this type of fracture usually starts close to the edge of the sample like a type 3, but tends to propagate at a similar angle to type 1. However, it is unlikely to occur frequently as the R/t ratio is quite high in most SMF applications. Shih and Shi [17] emphasized that this type of fracture is significantly sensitive to the restraining condition (F_2) or the tension level applied during the bending.

3.2 Fracture limit strain at outer surface (ϵ_{1f})

Figure 10 shows the effect of the ratio R/t on the fracture limit strain on the outer surface (ϵ_{1f}) of the samples subjected to different directions and test speeds. In a first analysis, the results indicated that ϵ_{1f} increased significantly with increasing R/t ratio. This behavior was due to the increase in the yield stress of the sample by strain hardening. In recent experimental studies, several researchers have observed the same tendency for other materials [42-45]. In general, the results showed that ϵ_{1f} reached its maximum value approximately in the range of $7.5 < R/t < 13.0$.

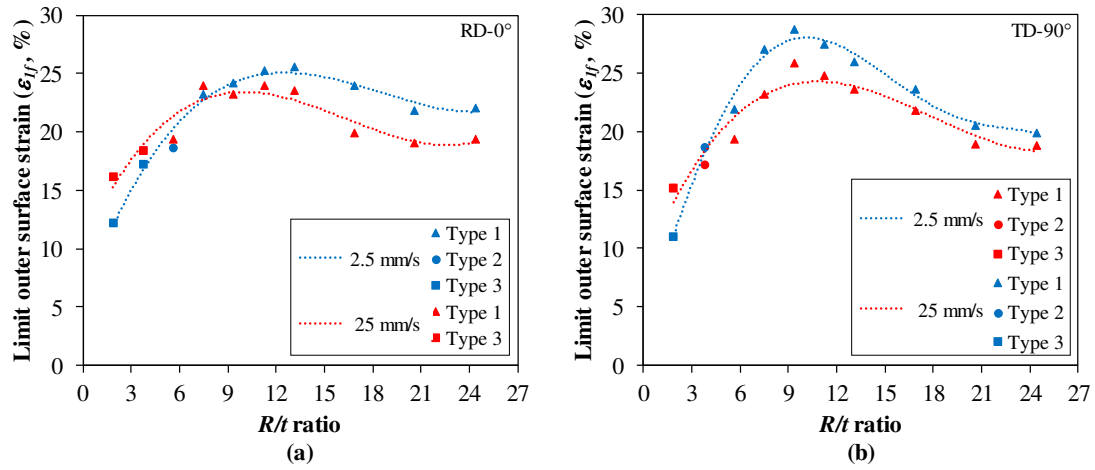


Fig. 10 Effect of R/t ratio on the fracture limit strain of outer surface (ϵ_{1f}) at different test velocity. (a) RD-0°; (b) TD-90°

Additionally, ϵ_{1f} decreased in both directions as the test speed increased. It is well known that in SMF processes the increase in velocity has a significant effect on the strain rate and, consequently, on the material properties. At room temperature, the work hardening of the material increases with increasing strain rate due to a more enhanced movement of dislocations, resulting in increased mechanical strength and decreased ductility of the material [27,38,39]. Yoshida et al. [46] demonstrated, through an analytical prediction of the behavior of metal sheets under stretching and bending, that ϵ_{1f} tends to be higher for materials with a high hardening coefficient (n); however, for a higher R/t ratio, this value tends to decrease, as stretching dominates the plastic deformation process. This reported behavior can be clearly seen in Figs. 10a and 10b, approximately from $R/t > 12.0$. At lower speeds, the TD direction ($\sim 9.0 < R/t < 12.0$) exhibited the highest possible value of ϵ_{1f} . These different behaviors can be attributed to the heterogeneity of the material properties. Supporting these arguments, Table 2 shows that the TD sample showed a higher anisotropy coefficient ($\sim 17\%$) than the RD sample, indicating that the sheet plane surface deforms more until necking and fracture occurred.

A more careful analysis of the results showed that as R/t increased, ϵ_{1f} tends to move from the curvature region to the flat region of the sheet, agreeing with the discussion in the previous section. Therefore, the sheet fracture mechanism changed from shear fracture in the punch radius to tensile fracture in the punch sidewall. This behavior has also been observed in studies of other materials [7,18,42]. Supporting these arguments, the macrographic images of the fractured samples (Figs. 5b–d) and the results shown in Fig. 10 demonstrated that type 1, type 2, and type 3 occurred when $R/t > 6.0$, $4.5 < R/t < 6.0$, and $R/t < 4.5$, respectively.

A comparative analysis between Figs. 10 and 1a revealed that the magnitudes of the deformations were very similar, indicating again that the DBF test effectively reproduced an SMF industrial operation. Therefore, these results could be

used as design guidelines and failure prevention criteria in the development of processes and products from FSS AISI 430. In addition, they can be used in the SMF processes to avoid problems related to conformability in the parts' radii.

3.3 Fracture limit strain of thickness (ϵ_{3f})

Figure 11 shows the effect of the ratio R/t on the fracture limit strain upon the thickness (ϵ_{3f}) of samples subjected to different directions and test speeds. From this figure, it is clear that ϵ_{3f} increases with an increase in the ratio R/t , i.e., the sheet thickness decreases. In this regard, Yoshida et al. [46] explained that during stretching and bending, the yield strength of the sheet (S_y) increases with the outer surface strain ϵ_{1f} because of its cold work hardening; however, the thickness of the sheet decreases. Since the sample is in a plane-strain state, this behavior obeys the law of volume constancy.

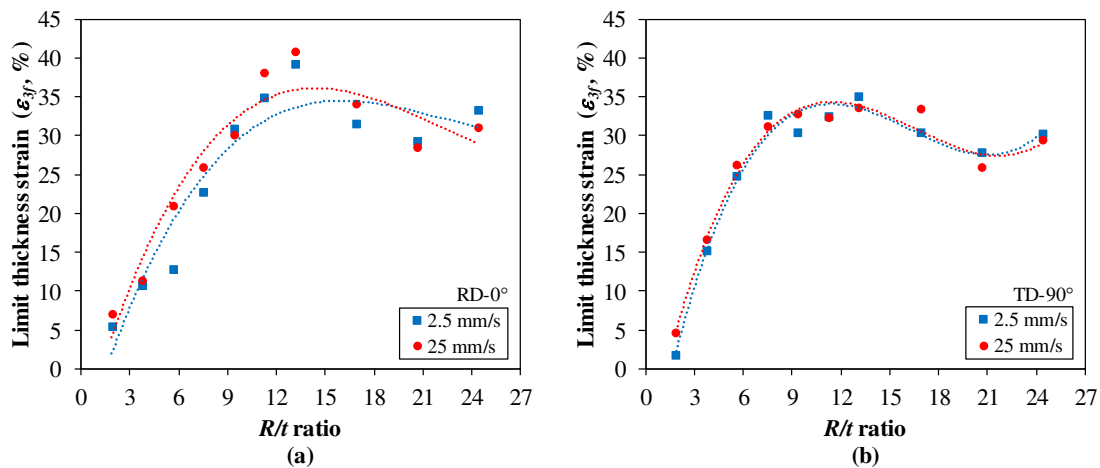


Fig. 11 Effect of the R/t ratio on the fracture limit strain of thickness (ϵ_{3f}) at different test velocity. (a) RD-0°; (b) TD-90°

A more careful analysis of the results showed that ϵ_{3f} tends to stabilize more quickly in e TD ($\sim R/t = 7.5$) than in the RD ($\sim R/t = 13.0$). This behavior was explained by the mechanical properties of the material (Table 2); the higher the normal anisotropy coefficient (r), the higher is the material's resistance to thinning, allowing the surface and wall of the plate to deform more until the fracture. The results also showed that when the R/t ratio was very low (≤ 1.5), type 3 occurred almost instantly, as there was practically no apparent necking in the sample section ($\epsilon_{3f} < 7\%$), indicating that the thickness strain ceased even before the sample reached uniform elongation. However, this behavior differed from that of type 1 because when R/t was high the ductility of the sheet still remained quite significant ($\epsilon_{3f} > 30\%$), even after

reaching the uniform elongation, ceasing only with the sample fracture. Increasing the test speed had a more significant effect on the RD, most likely due to its lower normal anisotropy coefficient; consequently, the thickness reduction tended to increase.

In summary, these results suggested that for predicting a fracture in SMF processes, the FLD is valid only for failures induced by necking on flat surfaces and under approximately proportional loading conditions. In this regard, Cheong [21] emphasized that nonlinear deformation trajectories and out-of-plane deformations are excluded from FLDs, which explains the unpredictability of the fracture of AISI 430 steel shown in Fig. 1.

3.4 Limit wall stretch (L_{max}/L_0)

Figure 12 shows the effect of the R/t ratio on the limit wall stretch of the samples subjected to different test directions and speeds. It is clearly noted that L_{max}/L_0 increased significantly with increasing R/t because of the lower strain hardening of the material as the bending severity decreased. According to the bending theory [27,38], the larger the radius of curvature, the smaller the decrease in sheet thickness in the bending region and, consequently, the higher the capacity of the sheet to stretch or deform longitudinally. Several researchers [17-20,46-49] have investigated the effect of the radius of curvature on the limit wall stretch of other materials and observed the same trend.

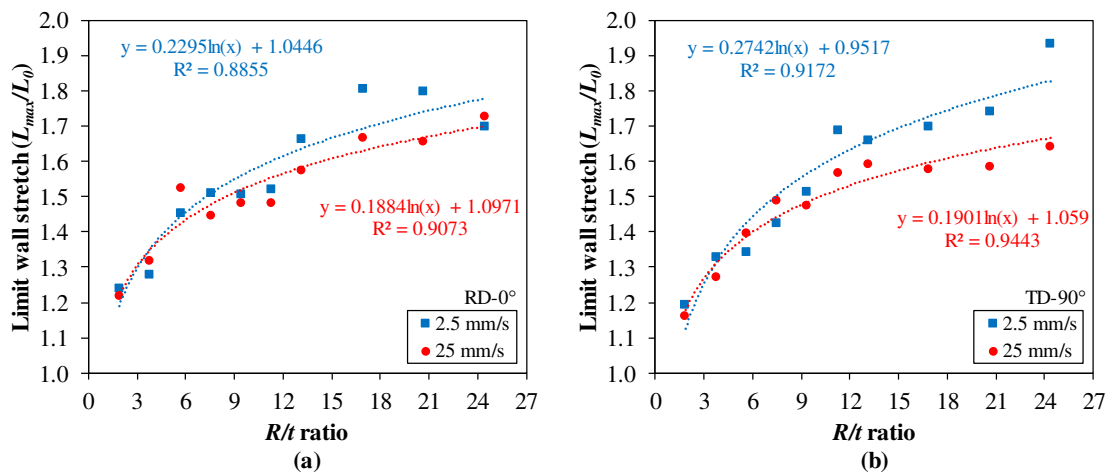


Fig. 12 Effect of the R/t ratio on the limit wall stretch (L_{max}/L_0) at different test velocity. (a) RD-0°; (b) TD-90°

Ma and Welo [50] explained that for most metallic materials during bending, the neutral line (NL) that separates the tensioned region from the compressed region moves away from the center of the sheet as the radius of curvature increases. Cheong [21] reported that this NL displacement for the out-plane has a positive influence on the formability of the sheet metal, as it provides a stronger deformation gradient in the layer under tension. Until the outer surface of the sheet reaches

its critical deformation limit, the inner layers that are under moderate tensile or compressive load provide stability to sheet thickness, mitigating the effects of necking and, consequently, increasing the limit wall stretch. Figure 11 confirms this necking behavior. As already mentioned, the deformation at thickness increased with increasing radius of curvature and tended to stabilize from a critical R/t ratio, but the sheet stretch continued to increase due to the work hardening of the material increasing less.

Additionally, the magnitude of L_{max}/L_0 decreased with an increase in the test speed. As discussed, increasing the strain rate caused the yield strength of the material to increase due to strain hardening, causing the magnitude of the stretch limit of the sheet to reduce. Fractures occur when all fibers close to the outer surface reach the limit strain (ϵ_{1f}) [44]. At high speed, both directions (RD and TD) showed very similar behavior; however, at low speed, the TD sample (Fig. 10b) exhibited a higher L_{max}/L_0 value, most likely, due to the higher resistance to thinning, which provided a greater stretching.

Therefore, the experimental results showed that the limit strain of the sheet metal (ϵ_{limit}) under bending and stretching is assumed as be the superposition of the bending limit deformation (ϵ_{bend}) and stretch ($\epsilon_{stretch}$). This suggests that the smaller the contribution of ϵ_{bend} in the plastic deformation process—this occurs with the displacement of the NL out of the plane as the ratio R/t increases—the more ϵ_{limit} approaches $\epsilon_{stretch}$ and, consequently, of FLD_0 . Considering this, industrial practice has produced thicker parts and with large bend radius to ensure success in SMF operations. However, these practices directly impact the other parameters; for example, an increase in the force required to deform a part, an increase in production costs, and an increase in the friction and wear process between the tribo-surfaces. Experimental analysis is a very powerful tool in this context, as it allows a more curated analysis of the physical phenomena involved in the plastic deformation process of a metallic sheet, which can determine more assertive solutions in developing processes and products.

3.5 Coefficient of friction (COF)

Figure 13 shows the effect of the R/t ratio on the COF of the samples subjected to different test directions and speeds. We noticed that the COF increased with a decrease in the pin radius; however, this behavior changed from a critical R/t ratio, from which the COF increased with an increase in the pin radius. Nanayakkara and Hodgson [30] observed a similar behavior for a galvanized steel sheet subjected to the BUT test and concluded that from a critical radius, the tribo-system changed from a mixed lubrication regime to a hydrodynamic lubrication regime. Andreasen et al. [51] explained that this change may be related to the varying contact pressure and sheet roughness due to the plastic strain by stretching.

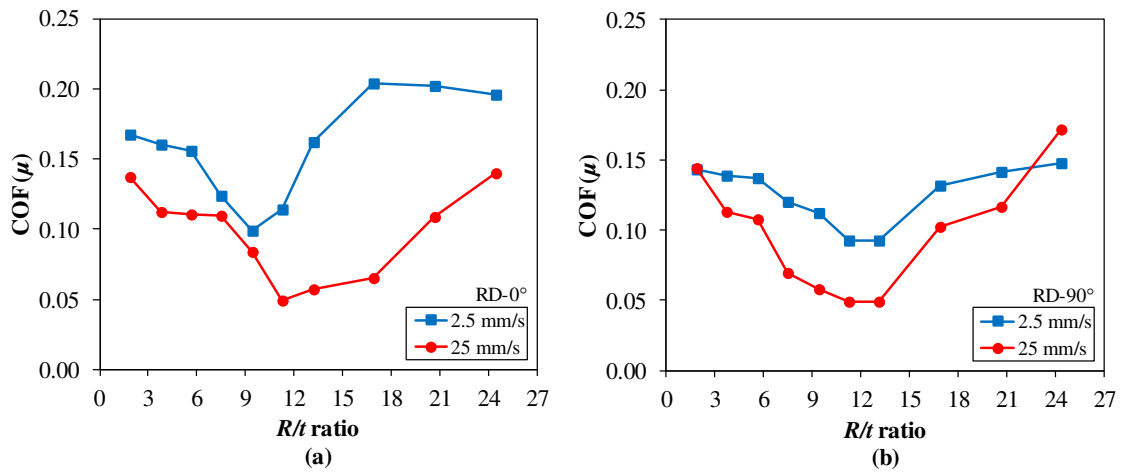


Fig. 13 Effect of the R/t ratio on the COF at different test velocity. (a) RD-0°; (b) TD-90°

Kim et al. [52] demonstrated that the contact pressure increases as the radius of the pin decreases; moreover, it is not uniformly distributed on the contact surface. According to the Stribeck curve, when the contact pressure increases (p), the lubricant viscosity (η) or speed (v) decrease [53]. Under these conditions, the ability of the lubricant to separate the contact surfaces and stabilize the COF is diminished [54]. Several authors [55-57] have reported that at higher pressures, the lubricating film can be expelled from the friction zone or break, increasing the interaction between the asperities of the tribo-surfaces and, consequently, the friction resistance. Once the sheet surface is softer (~ 4.8 times) than the bending pin, an increase in this interaction produces deep galling on the sheet surface and with material transfer, as shown in Fig. 14a. This suggests that the high level of friction and galling may have contributed to the occurrence of shear fracture. Figure 14b also supports these arguments by showcasing the different micro-effects of friction and wear mechanisms that governed the interface of the tribo-contact.

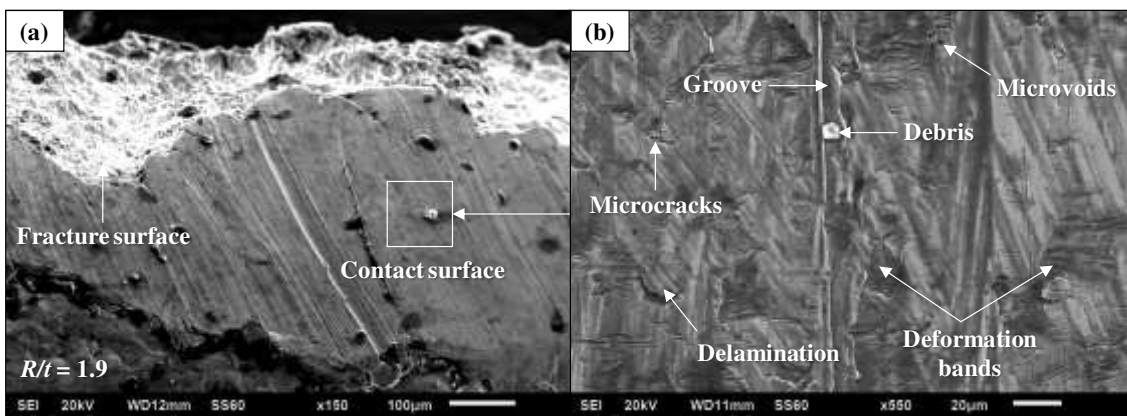


Fig. 14 SEM image showing (a) galling on the contact surface and the (b) effects of friction and wear mechanisms

Still according to the Stribeck curve, the COF in fluid-lubricated contacts is a nonlinear function with the Hersey number ($\eta v/p$) [53]. From a critical value of this number, the COF tends to increase continuously, suggesting that significant changes occur at the contact interface, which explains the increase in the COF from the R/t ratio critical. In SMF operations, the lubricating film is very thin; therefore, the lubrication regime is said to be micro-hydrodynamic [55]. This lubrication regime is very sensitive to topographical changes at the contact interface. Recent studies have shown that the surface roughness and COF increase as the relative elongation of the sheet increases [58,59]. This increase in surface roughness is explained by a theory about the formation of Lüders bands during the plastic deformation of steels with low carbon [60-62]. Makhkamov [63] emphasized that in addition to the plastic deformation altering the surface roughness, it also eliminates most of the elastic effects on contact and opens a new surface by the action of dislocation sliding.

However, the contribution of roughness to the tribo-system cannot be analyzed in isolation. It is well known that a higher surface roughness guarantees enhanced lubrication due to the presence of more valleys; however, this is true only to a certain extent, as varying the contact pressure affects the adhesion mechanisms and plastic strain of sheet asperities. Since sheet asperities are softer than tool asperities, at high pressures, they tend to undergo a greater degree of flattening and, consequently, adhesive forces, frictional resistance, and surface wear tend to increase.

In addition, several researchers [30-64] have demonstrated that the bending force is significant in friction analysis and, therefore, cannot be ignored. Eq. 6 shows that F_b decreases with increasing pin radius. According to Eq. 1, the force required to pull the strip (F_1) over the pin increases as F_b decreases, resulting in an increase in the normal load on the sheet surface that causes a greater degree of flattening of its asperities. Eq. 5 also supports these arguments.

The COFs obtained showed the same tendencies as other researchers [52,55] observed in their experiments, COF decreased as the test speed increased. At higher speeds, it was observed that the RD and TD samples presented very similar behaviors, suggesting that the COF became more independent of the contact pressure under this condition. The Stribeck curve also supports this argument [57]. This was because the lubrication regime at the contact interface became more similar to micro-hydrodynamic lubrication, where the load was carried more by the lubricating film.

However, at lower speeds, the COF in the RD direction was higher than that in the TD direction, most likely due to the heterogeneity in the texture of the AISI 430 steel sheet under plastic deformation. Shin et al. [65] explained that FSS exhibits striations parallel to the rolling direction when subjected to drawing or deep drawing operations. Generally, the striations have a depth in the range of 20–50 μm . Therefore, under these conditions, the distribution of the lubricant and the efforts are not uniform at the contact interface, which can cause different lubrication regimes in the same tribo-system and, as result, the friction resistance tends to increase.

4 Conclusions

The main conclusions obtained from the analysis of the experimental results are summarized below:

- The DBF test was able to reliably reproduce, under a plane-strain state, three different types of fractures in an AISI 430 sheet steel: type 1 (necking failure in the punch sidewall), type 2 (failure in the tangent point between the punch radius and sidewall), and type 3 (failure in the punch radius).
- The fracture limit strain on the outer surface increased with increasing R/t and, simultaneously, shifted and changed its typical characteristics. Tensile fracture occurred when $R/t > 6.0$, mixed fracture when $4.5 < R/t < 6.0$, and the shear fracture when $R/t < 4.5$. Their maximum values were approximately in the range of $7.5 < R/t < 13.0$.
- The fracture limit strain at the thickness increased with increasing R/t ; however, beyond a critical point in their relationship, it exhibited a tendency to stabilize. This indicated that the FLD was valid only for necking-induced failures on flat surfaces and under approximately proportional loading conditions.
- The wall stretch limit increased with increasing R/t , most likely due to lesser work hardening of the material. The increase in sheet resistance to thinning in the TD provided a more enhanced stretch than the RD.
- The COF increased with the decrease in the pin radius; however, this behavior changed from a critical R/t ratio, where the COF increased with increasing pin radius. Parameters, such as the variation of contact pressure, sheet surface roughness, bending force, and lubrication regime had a direct impact on the COF.
- Finally, these results can be used as design guidelines and failure prevention criteria in the development of processes and products from AISI 430 steel. In addition, they can be used to avoid failures related to conformability in parts' radii.

5 Acknowledgements

The authors would like to thank CEFET-MG and UFMG for their technical support and allowing the use of their equipment. The authors also thank Aperam South America, Timóteo, Minas Gerais, Brazil, for providing the steel sheet samples of the steel sheet used in this study. In addition, the authors thank Golden Inox company from drawing of the example-part.

6 Declarations

Funding: Not applicable for that section.

Conflicts of interest/Competing interests: The authors declare that they have no known competing financial interests or personal relationships that could have appeared to influence the work reported in this paper.

Availability of data and material: All data generated or analysed during this study are included in this published paper. Requests for material should be made to the corresponding authors.

Authors' contributions: Luiz VD - Resources, Methodology, Investigation, Data Curation, Writing - Original Draft. Rodrigues PCM - Resources, Conceptualization, Methodology, Writing - Review & Editing, Supervision, Project administration, Formal analysis, Funding acquisition.

Ethics approval: Not applicable for that section.

Consent to participate: Not applicable for that section.

Consent for publication: Not applicable for that section.

7 References

1. ASTM A240/A240M-20a (2020) Standard specification for chromium and chromium-nickel stainless steel plate, sheet, and strip for pressure vessels and for general applications. ASTM International, West Conshohocken, PA
2. Krauss G (2005) Steels: Processing, Structure and Performance. 1st ed. Ohio: ASM International
3. ISSF (2007) The ferritic solution: properties, advantages, applications. https://www.worldstainless.org/Files/issf/non-image-files/PDF/ISSF_The_Ferritic_Solution_English.pdf. Accessed 27 Apr 2021
4. Lo KH, Shek CH, Lai JKL (2009) Recent developments in stainless steels. Mater Sci Eng Rep 65(4-6):39-104. <https://doi.org/10.1016/j.mser.2009.03.001>
5. Keeler SP, Backofen WA (1964) Plastic Instability and Fracture in Sheets Stretched Over Rigid Punches. ASM Trans Q 56(11):25-48
6. Marciniak Z, Kuczynski K (1967) Limit Strains in the Process of Stretch Forming Sheet Metal. Int J Mech Sci 9(9):609-612. [https://doi.org/10.1016/0020-7403\(67\)90066-5](https://doi.org/10.1016/0020-7403(67)90066-5)
7. Sung JH, Kim JH, Wagoner RH (2012) The Draw-Bend Fracture Test and Its Application to Dual-Phase and Transformation Induced Plasticity Steels. J Eng Mater Technol 134(4):041015. <https://doi.org/10.1115/1.4007261>

8. Scales M, Tardif N, Kyriakides S (2016) Ductile failure of aluminum alloy tubes under combined torsion and tension. *Int J Solids Struct* 97-98:116–128. <https://doi.org/10.1016/j.ijsolstr.2016.07.038>
9. Roth CC, Mohr (2018) Determining the strain to fracture for simple shear for a wide range of sheet metals. *Int J Mech Sci* 149:224–240. <https://doi.org/10.1016/j.ijmecsci.2018.10.007>
10. Kim JH, Sung, JH, Kun P, Wagoner RH (2011) The Shear Fracture of Dual-Phase Steel. *Int J Plast* 27:1658–1676. <https://doi.org/10.1016/j.ijplas.2011.02.009>
11. Park N, Stoughton TB, Yoon JW (2020) A new approach for fracture prediction considering general anisotropy of metal sheets. *Int J Plast* 124:199–225. <https://doi.org/10.1016/j.ijplas.2019.08.011>
12. Ferreira Filho A, Herrera C, Lima NB, Plaut RL, Padilha AF (2007) Texture evolution of ferritic (AISI 430) stainless steel strips during cold rolling, annealing and drawing. *Mater Sci Forum* 539–543:4926–4931. <https://doi.org/10.4028/www.scientific.net/MSF.539-543.4926>
13. Raabe D, Lücke K (1993) Textures of ferritic stainless steel. *Mater Sci Technol* 9(4):302–312. <https://doi.org/10.1179/mst.1993.9.4.302>
14. Labiapari WS, Ardila MAN, Costa HL, Mello JDB (2019) Abrasion-corrosion of ferritic stainless steel. In: Duriagina Z, editor. *Stainless steels and alloys*. 1st ed. London: IntechOpen; <https://doi.org/10.5772/intechopen.81913>
15. Damborg FF (1999) Bending-Under-Tension Formability: -A comparison between aluminium and steel. PhD Dissertation, Aalborg University
16. Walp MS, Wurm A, Siekirk III JF, Desai AK (2006) Shear Fracture in Advanced High Strength Steels. *SAE Tech Pap* 2006-01-1433. <https://doi.org/10.4271/2006-01-1433>
17. Shih H-C, Shi MF (2008) Experimental study on shear fracture of advanced high strength steels. *Proceedings of the 2008 International Manufacturing Science and Engineering Conference*; 2008 Oct 7-10; Evanston, Illinois, USA. New York: ASME International; p. 41–47. https://doi.org/10.1115/MSEC_ICMP2008-72046
18. Shih H-C, Shi MF, Xia ZC, Zeng D (2009) Experimental study on shear fracture of advanced high strength steels: Part II. *Proceedings of the 2009 International Manufacturing Science and Engineering Conference*; 2009 Oct 4-7; West Lafayette, Indiana, USA. New York: ASME International; p. 513–519. <https://doi.org/10.1115/MSEC2009-84070>
19. Ghosh AK, Hecker SS (1974) Stretching limits in sheet metals: In-plane versus out-of-plane deformation. *Metall Trans B* 5(10):2161–2164. <https://doi.org/10.1007/BF02643929>
20. Baudelet B, Ragab AR (1982) Forming limit curves: Out-of-plane and in-plane stretching. *J Mech Work Technol* 6(4):267–276. [https://doi.org/10.1016/0378-3804\(82\)90027-4](https://doi.org/10.1016/0378-3804(82)90027-4)
21. Cheong D-WK (2019) On the Influence of the Through-Thickness Strain Gradients for Characterization of Formability and Fracture of Sheet Metal Alloys. PhD Dissertation, University of Waterloo

22. Narayanaswamy OS, Demeri MY (1983) Analysis of the Angular Stretch Bend Test: Novel Techniques in Metal Deformation Testing. The Metallurgical Society, St. Louis, MO 99–112
23. Wenzloff GJ, Hylton TA, Matlock DK (1992) Technical Note: A New Test Procedure for the Bending under Tension Friction Test. *J Mater Eng Perform* 1(5):609-614. <https://doi.org/10.1007/BF02649242>
24. Vallance DW, Matlock DK (1992) Application of the bending-under-tension friction test to coated sheet steels. *J Mater Eng Perform* 1(5):685–693. <https://doi.org/10.1007/BF02649250>
25. Marcianik Z, Duncan JL, Hu SJ (2002) *Mechanics of Sheet Metal Forming*. 1st ed. Oxford: Butterworth-Heinemann;
26. ASTM E8/E8M-16a (2016) Standard test methods for tension testing of metallic materials, ASTM International, West Conshohocken, PA, USA
27. Banabic D, Bunge H-J, Pöhlandt K, Tekkaya AE (2000) *Formability of metallic materials: Plastic Anisotropy, Formability Testing, Forming Limits*. Springer, Berlin
28. Purohit Z (2010) Performance of polymer coatings under forming conditions. PhD Dissertation, Texas A&M University
29. Loadstar Sensors (2020) RAS1 S Beam Load Cell, <https://www.loadstarsensors.com/assets/specsheets/ras1.pdf>; 2020. Accessed 8 January 2022
30. Nanayakkara NKBMP, Kelly G, Hodgson P (2005) Application of bending under tension test to determine the effect of tool radius and the contact pressure on the coefficient of friction in sheet metal forming. *Mater Forum* 29(1):114–118
31. Luiz VD, Rodrigues PCM (2022) Design of a Tribo-Simulator for Investigation of the Tribological Behavior of Stainless-Steel Sheets Under Different Contact Conditions. *Mater Res* 25:e20210220. <https://doi.org/10.1590/1980-5373-MR-2021-0220>
32. Silva MB, Isik K, Tekkaya AE, Martins PAF. Fracture Loci in Sheet Metal Forming: A Review. *Acta Metall Sin.* 2015;28(12):1415–1425. 10.1007/s40195-015-0341-6.
33. Parniere P, Sanz G (1976) *Appréciation des Caractéristiques d'Emboutissabilité des Tôles Minces – Mise en forme des métaux et alliages*. Centre National de la Recherche Scientifique–CNRS, Paris
34. ISO 12004-2 (2021). *Metallic materials—Sheet and strip—Determination of forming-limit curves—Part 2: Determination of forming-limit curves in the laboratory*; ISO standards, Geneva
35. Nielsen CV, Martins PAF (2021) *Metal Forming: Formability, Simulation, and Tool Design*. 1st ed. Elsevier, London
36. Trzepieciński T, Lemu G (2015) Proposal for an Experimental-Numerical Method for Friction Description in Sheet Metal Forming. *J Mech Eng* 61(6):383–391. <https://doi.org/10.5545/sv-jme.2015.2404>
37. Swift HW (1948) Plastic bending under tension. *Engineering* 166:333–359.
38. Dieter G. (1989) *Mechanical Metallurgy*. 3rd ed. McGraw Hill, New York

39. Li H, Fu M (2019) *Deformation-Based Processing of Materials: Behavior, Performance, Modeling, and Control*. 1st ed. Elsevier, Amsterdam
40. Martínez-Donaire AJ, Morales-Palma D, Vallellano C (2020) On the Use of Strain Path Independent Metrics and Critical Distance Rule for Predicting Failure of AA7075-O Stretch-Bend Sheets. *Metals* 13:3660. <https://doi.org/10.3390/ma13173660>
41. Bitzek E, Kermode JR, Gumbsch P (2015) Atomistic aspects of fracture. *Int J Fract* 191:13–30. <https://doi.org/10.1007/s10704-015-9988-2>
42. Tharrett MR, Stoughton TB (2003) Stretch-bend forming limits of 1008 AK steel. SAE Tech Pap 2003-01-1157. <https://doi.org/10.4271/2003-01-1157>
43. Luo M, Wierzbicki T (2010) Numerical failure analysis of a stretch-bending test on dual-phase steel sheets using a phenomenological fracture model. *Int J Solids Struct* 47:3084–3102. <https://doi.org/10.1016/j.ijsolstr.2010.07.010>
44. Morales-Palma D, Vallellano C, García-Lomas FJ (2013) Assessment of the effect of the through thickness strain/stress gradient on the formability of stretch-bend metal sheets. *Mater Des* 50:798-809. <https://doi.org/10.1016/j.matdes.2013.03.086>
45. Min J, Stoughton TB, Carsley JE, Lin J (2016) Compensation for process-dependent effects in the determination of localized necking limits. *Int J Mech Sci* 117:115-134. <https://doi.org/10.1016/j.ijmecsci.2016.08.008>
46. Yoshida M, Yoshida F, Konishi H, Fukumoto K (2005) Fracture limits of sheet metals under stretch bending. *Int J Mech Sci* 47(12):1885–1896. <https://doi.org/10.1016/j.ijmecsci.2005.07.006>
47. He J, Xia ZC, Zhu X, Zeng D, Li S (2013) Sheet metal forming limits under stretch-bending with anisotropic hardening. *Int J Mech Sci* 75:244–256. <https://doi.org/10.1016/j.ijmecsci.2013.07.007>
48. Neuhauser FM, Terrazas O, Manopulo N, Hora P, Van Tyne C (2019) The bending dependency of forming limit diagrams. *Int J Mater Form* 12:815–825. <https://doi.org/10.1007/s12289-018-1452-1>
49. Gihyun BG, Park N, Song J, Lee J, Jang I, Park K, Seo Y, Oh K (2020) Stretch-bending crack simulation for advanced high-strength thick steel sheets considering the contact pressure effect. *Procedia Manuf* 50:574–578. <https://doi.org/10.1016/j.promfg.2020.08.103>
50. Ma J, Welo T (2021) Analytical springback assessment in flexible stretching bending of complex shapes. *Int J Mach Tools Manuf* 160:103653. <https://doi.org/10.1016/j.ijmachtools.2020.103653>
51. Andreasen JL, Olsson DD, Chodnikiewicz K, Bay N (2006) Bending under tension test with direct friction measurement. *Proc Inst Mech Eng B J Eng Manuf* 220(1):73–80. <https://doi.org/10.1243/095440505X32913>
52. Kim YS, Jain MK, Metzger DR (2012) Determination of pressure-dependent friction coefficient from draw-bend test and its application to cup drawing. *Int J Mach Tools Manuf* 56:69–78. <https://doi.org/10.1016/j.ijmachtools.2011.12.011>

53. Jeyaprakash N, Che-Hua Y (2020) Friction, Lubrication, and Wear. In: Patnaik A, Singh T, Kukshal V, editors. Tribology in Materials and Manufacturing. 1st ed. IntechOpen, London. <https://doi.org/10.5772/intechopen.93796>
54. Trzepiecinski T, Lemu HG (2020) Effect of Lubrication on Friction in Bending under Tension Test-Experimental and Numerical Approach. *Metals* 10(4):544. <https://doi.org/10.3390/met10040544>
55. Roizard X, Raharijaona F, von Stebut J, Belliard P (1999) Influence of sliding direction and sliding speed on the micro-hydrodynamic lubrication component of aluminium mill-finish sheets. *Tribology International* 32:739–747. [https://doi.org/10.1016/S0301-679X\(00\)00008-6](https://doi.org/10.1016/S0301-679X(00)00008-6)
56. Bart JCJ, Gucciardi E, Cavallaro S (2013) *Biolubricants: Science and Technology*. 1st ed. Woodhead Publishing, Sawston
57. Blau PJ (2008) *Friction science and technology: from concepts to applications*. 2nd ed. CRC Press, Florida
58. Trzepiecinski T (2019) A study of the coefficient of friction in steel sheets forming. *Metals* 9(1):1–11. <https://doi.org/10.3390/met9090988>
59. Luiz VD, Rodrigues PCM (2021) Effect of the test conditions on tribological behavior of an Nb-stabilized AISI 430 stainless steel sheet. *J Braz Soc Mech Sci* 43:505. <https://doi.org/10.1007/s40430-021-03235-7>
60. Piobert A (1842) Expériences sur la pénétration des projectiles dans le fer forgé. *Mémoire L'artillerie* 5:502
61. Lüders W (1860) Ueber die auerung der elasticität an stahlartigen eisenstäben und stahlstäben, und über eine beim biegen solcher stäbe beobachtete molecularbewegung. *Dingler Polytech J* 155:18–22
62. Brlić T, Rešković S, Vodopivec F, Jandrić I (2018) Lüders bands at the beginning of the plastic flow of materials. *Metalurgija* 57(4):357-359
63. Makhkamov A, Wagre D, Baptista AM, Santos AD, Malheiro L. (2017) Tribology Testing to Friction Determination in Sheet Metal Forming Processes. *Cienc e Tecnol dos Mater* 29:249–253. <https://doi.org/10.1016/j.ctmat.2016.07.002>
64. Purohit Z, Zhanga Y, Wang J (2015) On surface damage of polymer coated sheet metals during forming. *J Manuf Process* 20(2):389–396. <https://doi.org/10.1016/j.jmapro.2014.09.002>.
65. Shin HJ, An JK, Park SH, Lee DN (2003) The effect of texture on ridging of ferritic stainless steel. *Acta Mater* 51(16):4693-4706. [https://doi.org/10.1016/S1359-6454\(03\)00187-3](https://doi.org/10.1016/S1359-6454(03)00187-3).